

Article

Validation of the Satellite Method for Measuring Spectra of Spatially Inhomogeneous Sea Waves

Valery Bondur¹, Vladimir Dulov^{1,2} , Vladimir Kozub¹, Alexander Murynin^{1,*} , Maria Yurovskaya^{1,2} 
and Yury Yurovsky^{1,2} 

¹ AEROCOSMOS Research Institute for Aerospace Monitoring, 105064 Moscow, Russia

² Remote Sensing Department, Marine Hydrophysical Institute of RAS, 299011 Sevastopol, Russia

* Correspondence: amurynin@bk.ru

Abstract: A method for retrieving 2D spatial spectra of sea wave elevations and slopes from high resolution (about 1 m) satellite imagery has been developed that also allows for assessing sea wave angular distributions. A validation of the suggested method was carried out based on the results from a comprehensive experiment that included both satellite imaging of the Black Sea water area and sea truth under controlled conditions. The retrieval of spatial wave spectra from fragments of a satellite image and comparison with the results of measuring the frequency spectra from sea truth data obtained using an array of string wave recorders were carried out. Wave spectra from remote and in situ data are consistent in the frequency range of 0.2–1.1 Hz, corresponding to wavelengths from 1.3 to 39 m.

Keywords: sea wave spectra; satellite imagery; remote measurement validation



Citation: Bondur, V.; Dulov, V.; Kozub, V.; Murynin, A.; Yurovskaya, M.; Yurovsky, Y. Validation of the Satellite Method for Measuring Spectra of Spatially Inhomogeneous Sea Waves. *J. Mar. Sci. Eng.* **2022**, *10*, 1510. <https://doi.org/10.3390/jmse10101510>

Academic Editor: Guido Benassai

Received: 29 September 2022

Accepted: 12 October 2022

Published: 17 October 2022

Publisher's Note: MDPI stays neutral with regard to jurisdictional claims in published maps and institutional affiliations.



Copyright: © 2022 by the authors. Licensee MDPI, Basel, Switzerland. This article is an open access article distributed under the terms and conditions of the Creative Commons Attribution (CC BY) license (<https://creativecommons.org/licenses/by/4.0/>).

1. Introduction

Sea wave spectra are important for studying many processes and phenomena occurring in seas and oceans [1,2]. They can be used to detect various types of anthropogenic and natural impacts on marine areas [3–6]. They also have important applications for human activities at sea and on the coast because surface waves affect shipping and harbor operations. The newest application is associated with the use of waves as a source of ocean renewable energy (e.g., [7]).

The spatial distribution of wave spectra parameters is used for detecting and recovering sea currents [8,9], bathymetry [8,10], and mesoscale ocean features [11,12]. The satellite remote sensing of sea waves is a highly perspective trend in ocean observing systems [2,13,14]. Wave directional spectra and patterns of spatial distributions of wave parameters are modern challenges in remote technologies [1,8,13,14].

To measure wave spectra, in situ data are usually applied, obtained using wave recorders installed on special platforms or buoys. Such data allow us to obtain temporal and angular characteristics of sea surface wave spectra at a given point of the sea surface over certain time intervals. In turn, the retrieval of wave spectra from satellite images makes it possible to obtain a one-time spectral characteristic of waves for a large water area [3,15,16]. Moreover, this approach facilitates the study of offshore water areas [17,18].

The complexity of the problem of retrieving the spectra of sea waves based on satellite data is associated with a large number of factors that affect both the processes of wave generation and the formation of the satellite images themselves [3]. Special retrieving operators [15,19,20], taking into consideration various parameters of imaging and light conditions, were developed for retrieving wave spectra using optical imagery.

When constructing mathematical operators that retrieve the spectra of sea surface slopes, the physical mechanisms involved in the formation of sea surface brightness fields and their spectra are taken into account.

Here, we focused on the development and validation of the method for remote measuring variations related to the spatial and temporal inhomogeneity of sea waves.

This paper presents a case study on retrieving and validating the wave spectra from optical satellite imagery. Section 2 discusses methods for image processing and in situ data acquisition including a comprehensive experiment on ground-truth measurements during satellite imagery. Section 3 focuses on the measurement results and reveals the effects of the spatio-temporal variability of the observed sea state. Section 4 discusses these issues with an explanation of some results. Section 5 summarizes the paper.

2. Methods and Materials

2.1. The Features of the Method of Remote Measurement of Wave Spectra

An approach has been developed for retrieving the spatial spectra of slopes and elevations of surface waves from aerospace optical images, which takes into account the nonlinear modulation of the brightness field by the slopes of the sea surface and includes the parameterization of spatial-frequency filters using a set of parameters depending on a set of conditions.

Since the elevation of the rough sea surface (the water–air interface) at each point changes randomly depending on the coordinates and time, here, we used the concept of a field to describe this surface. The field is a random function of several variables (coordinates and time).

Rough sea surface is a field of elevations, $z = \zeta(x, y, t)$, where (x, y, z) is the rectangular coordinate system in which the horizontal (x, y) plane corresponds to the calm state of the sea, and t is the current moment of time.

When measuring wave spectra remotely, the source of information is satellite images, therefore considered to be instantaneous and created at the moment of time, t_s . For further discussion, it is convenient to use the expression

$$z = \zeta(x, y) = \zeta(x, y, t_s). \tag{1}$$

It is known that the state of sea waves is quite fully described using the spatial and frequency energy spectra of sea waves [1]. Methods for remote measurement of these spectra are being actively developed [3,15–17,19–22].

Measuring the spatial energy spectrum of waves physically means building the spectral density of waves that is a function describing the distribution of the power of waves depending on the wavenumber vector. In this case, the wave power per unit interval of spatial frequencies (or proportional to their wave numbers) is to be determined.

Spectral density of the elevation field is proportional to the squared modulus of the Fourier transform of this field:

$$\Psi(\mathbf{k}) = c \cdot |F[z]|_2, \tag{2}$$

where c is the constant factor determined by the size of the investigated surface area, $F[\cdot]$ is the Fourier transform, and $\mathbf{k} = (k_x, k_y)$ is the wave vector.

Satellite images used for retrieving spatial wave spectra, $\Psi(\mathbf{k})$, register brightness fields generated by electromagnetic radiation in the visible range, reflected and refracted on a rough water surface. Since the reflection and refraction of light occurs according to the laws of geometric optics, the brightness of the sea surface element is determined not by the elevation of this element relative to the average level of the surface, but by its angles of inclination relative to the horizontal plane, and these angles are directly related to the gradients of the elevation field (i.e., the field of slopes of the sea surface):

$$\nabla_{\zeta}^{\phi_C}(x, y) = \frac{\partial \zeta(x, y)}{\partial x} \cdot \cos \phi_C + \frac{\partial \zeta(x, y)}{\partial y} \cdot \sin \phi_C \tag{3}$$

where ϕ_C is the angle that has a physical meaning of the average direction of the sea surface illumination gradient in the (x, y) plane, which is determined from the illumination conditions.

In the general case, the dependence of the brightness field on the slope field includes linear and nonlinear components [15]:

$$B(x, y) = C \left(\frac{\partial \zeta(x, y)}{\partial x} \cdot \cos \phi_C + \frac{\partial \zeta(x, y)}{\partial y} \cdot \sin \phi_C \right) + N(x, y, \nabla \zeta) \tag{4}$$

where N is the brightness field component having nonlinear dependence on surface slopes; C is the constant determined by the imaging conditions.

Based on the arguments above, an approach was used that is based on the construction of a retrieving operator \mathbf{R} , for the transition from the spectral density of the brightness field, $S(\mathbf{k})$, to the spectral density of the slope field [15]:

$$\Phi_{\phi_C}(\mathbf{k}) = \mathbf{R}(\mathbf{W})S(\mathbf{k}) \tag{5}$$

where $\Phi_{\phi_C}(\mathbf{k})$ is the spectral density of the slope field:

$$\Phi_{\phi}(\mathbf{k}) = |F[\nabla \zeta_{\phi}]|^2 \tag{6}$$

Moreover, this operator, \mathbf{R} , may depend on the set of parameters, \mathbf{W} , determined by the survey conditions and the characteristics of the imaging equipment [3].

Since the task is difficult for an analytical solution, direct numerical modeling of sea surface images and the calculation of wave spectra distortions are used to obtain the operator, \mathbf{R} . Numerical simulation takes into account the following characteristics [15,19,23,24].

- Distribution of the intensity of radiation coming from the upper hemisphere and reflected by the sea surface;
- Multiple scattering in the water column of radiation passing through the surface;
- Scattering of radiation by the roughness of surface elements.

As a result of the studies, the parameters were determined that significantly affect the characteristics of the retrieving operator, developed for measuring sea wave spectra from remote sensing data. These parameters are:

- An angle between the sun vector and the line of sight (when shooting in nadir, this angle coincides with the angle between the sun vector and the vertical);
- Image spatial resolution (geometric pixel size);
- Exponent of power-law approximation of the spectrum of sea surface elevations.

To adequately apply the multi-parameter retrieving operator under various wave formation conditions, the parameters were previously refined in [17,19,20]. To do this, we used the results of the comparison of remotely measured spectra of the rough sea surface with the data of sea truth measurements, which were carried out using sensors installed on a stationary hydrophysical platform and on floating buoys [17,18]. As a result of comparison in the range of power-law decay of the frequency spectrum, a correction for the parameters of the retrieving operator was previously obtained. The resulting correction corresponds to wave formation in the water area, where mixed waves are observed including both wind waves under the conditions of large fetch and swell waves [17–19].

The spectral density of the slope field (6) is related to the elevation field spectrum [3,19]:

$$\Phi_{\phi}(\mathbf{k}) = (k_x \cdot \cos \phi + k_y \cdot \sin \phi)^2 \Psi(\mathbf{k}) \tag{7}$$

Then, the unknown elevation field spectral density (1) can be found from the equation:

$$\Psi(\mathbf{k}) = \mathbf{R}(\mathbf{W})S(\mathbf{k}) / (k_x \cdot \cos \phi_C + k_y \cdot \sin \phi_C)^2 \tag{8}$$

Note, that Equation (8) does not allow us to determine the density value in the vicinity of directions orthogonal to the ϕ_C direction, because in this case, the denominator tends to zero. To overcome this shortcoming, if stereo imaging is available or light conditions

are different in different parts of the image, one can use the multi-position approach [24]; however, its use in satellite images is associated with certain technical difficulties [19].

Here, we used the operator, **R**, which is a frequency-spatial filter that retrieves the wave spectrum in the high-frequency and low-frequency regions of the spectrum [15].

The quality of the **R** operator’s work and of the selected parameters was tested in a number of experiments, where good agreement with the sea truth data was demonstrated [16,17,19,20].

In this paper, the problem of validating this operator under conditions of spatially inhomogeneous waves was considered.

2.2. Sea Truth Methods Used to Validate the Method for Remote Measurement of Wind Wave Spectrum

The purpose of wave record processing is to obtain estimates of the frequency-angular spectrum of waves, presented, for convenience, as follows:

$$S(f, \vartheta) = S(f)A(f, \vartheta), \tag{9}$$

where f is the frequency; ϑ is the wave travel direction; and the frequency spectrum is related to the height of significant waves as follows:

$$H_S = 4 \sqrt{\int_0^\infty S(f)df}, \tag{10}$$

Angular wave distribution fits the following condition:

$$\int_0^{2\pi} A(f, \vartheta)d\vartheta = 1. \tag{11}$$

Following the recommendations for wave data processing [25], we used the representation of the angular distribution in the form of a truncated Fourier expansion [26,27]:

$$A(f, \vartheta) = \frac{1}{\pi} \left(\frac{1}{2} + a_1(f) \cos \vartheta + b_1(f) \sin \vartheta + a_2(f) \cos 2\vartheta + b_2(f) \sin 2\vartheta \right). \tag{12}$$

Then, the angular distribution of waves is characterized by four main parameters—average direction of the waves, ϑ_M , general direction of the waves, ϑ_G , width of the angular distribution, determined through the amplitudes of the first or second harmonics, σ_1 and σ_2 [25,27]:

$$\vartheta_M(f) = \text{atan}(b_1/a_1) \tag{13}$$

$$\vartheta_G(f) = \text{atan}(b_2/a_2)/2 \tag{14}$$

$$\sigma_1(f) = \sqrt{2 \left(1 - \sqrt{a_1^2 + b_1^2} \right)}, \tag{15}$$

$$\sigma_2(f) = \sqrt{\frac{1}{2} \left(1 - \sqrt{a_2^2 + b_2^2} \right)} \tag{16}$$

The frequency spectrum and parameters of angular distribution were obtained from six wave recorders using the method of heave/slope triplet analysis [25,27,28]. The surface elevations from the six wave sensors were least-square-approximated by a plane to obtain the time series of wave elevation and two wave slopes corresponding to triplet measurements from wave buoys.

We calculated auto- and cross-spectra of elevations and two slopes according to the standard method by Fourier transform using the Hann window (e.g., [29]). The spectra were calculated from twenty-minute fragments and had 22 degrees of freedom. Further-

more, following the processing method [25], the coefficients of the angular distribution were estimated:

$$a_1(f) = \frac{\text{Im}(S_{0X}(f))}{kS(f)} \tag{17}$$

$$b_1(f) = \frac{\text{Im}(S_{0Y}(f))}{kS(f)} \tag{18}$$

$$a_2(f) = \frac{S_{XX}(f) - S_{YY}(f)}{k^2S(f)} \tag{19}$$

$$b_2(f) = \frac{\text{Re}(S_{XY}(f))}{k^2S(f)} \tag{20}$$

where S_{0X} , S_{0Y} , S_{XX} , S_{YY} , and S_{XY} are the frequency cross-spectra of elevations and slopes in the X and Y orthogonal direction, autospectra, and the cross-spectrum of slopes, respectively; k is the wavenumber related with the frequency through the dispersion relation for linear waves in deep water in the absence of currents.

$$k = \omega^2/g, \tag{21}$$

where g is the gravity and $\omega = 2\pi f$ is the circular frequency.

The dispersion relation can also be estimated from the obtained data [26,27]:

$$k_*(f) = \sqrt{\frac{S_{XX}(f) + S_{YY}(f)}{S(f)}}. \tag{22}$$

Comparison of such an estimate with the dispersion relation (21) makes it possible to judge the quality of the data. Previously, the same analysis was applied to the interpretation of wave measurements from an offshore platform [30] and the validation of minibuoy measurements using a wave recorder array [31]. It should be noted that the relations (17)–(20) are valid only in the absence of currents [26].

Estimation of the Current Velocity Vector in the Near-Surface Layer from Video Records

The current velocity estimation algorithm was used, which was described and verified in [21]. We obtained a 3D frequency-wavenumber spectrum from a video record of the sea surface (e.g., [32]). The spectrum frequency slices corresponding to frequencies ranging from 0.7 Hz to 1.2 Hz were cross-correlated with all possible sample slices simulated for the expected magnitude of current velocities (<1 m/s with 0.05 m/s step for both zonal and meridional components). As a result, we derived the effective current velocity estimate based on the optimal recognition of the dispersion shell signature in the spectrum. This process minimizes the impact of spurious spectral artifacts due to sun glints, foam, marine debris, etc. The effective velocity is the weighted mean over the wave penetration depth (e.g., [33]). For the selected wave frequency range, our velocity estimate roughly corresponded to the mean current in the upper 0.1 m layer.

According to the video record of the sea surface, the current velocity in the near-surface water layer did not exceed 2.5 ± 1.5 cm/s. Measurements of the current velocity at depths of 5, 10, 15, and 20 m using current recorders showed the velocities at the time of the satellite passage, respectively, to be 5.6, 1.7, 4.6, and 4.1 cm/s directed 40, 29, 32, and 35 degrees, respectively. Thus, at the time of the experiment, there were practically no currents at the location of the platform. This gives grounds for the analysis of wave measurements performed from a fixed platform to apply the dispersion relation for gravity waves in the absence of currents (21).

2.3. An Approach to Validation of the Method for Remote Measurement of Wind Wave Spectra Using Sea Truth Measurements

To calibrate and check the adequacy of the remote measurement method, we used in situ data obtained by synchronous recording of wave spectra using an array of string wave recorders. In this case, the spectra obtained by different measurement methods were compared.

A general technique for processing satellite images and sea truth data to validate the remote method for retrieving characteristics of a rough sea surface was proposed in [16,19,20].

To validate the method for retrieving the spatial spectra of the sea surface from satellite images, complex experiments were performed including satellite survey of the test water area and synchronous sea truth measurements from a stationary oceanographic platform using an array of string wave recorders. To select the parameters of the retrieving operator, R , the sea wave spectra measured by remote methods and in situ were compared.

To do this, the following actions were performed: calculation of the spatial spectrum of the selected image fragment closest to the point of sea truth measurements; retrieval of the spectrum of surface slopes using the retrieving operator, $R(W)$, constructed for a set of conditions determined by the conditions for satellite survey; calculation of the spatial spectrum of elevations from the retrieved spectrum of slopes; and recalculation into the frequency spectrum, taking into account the dispersion relation of gravity waves.

A flowchart illustrating the described technique is shown in Figure 1.

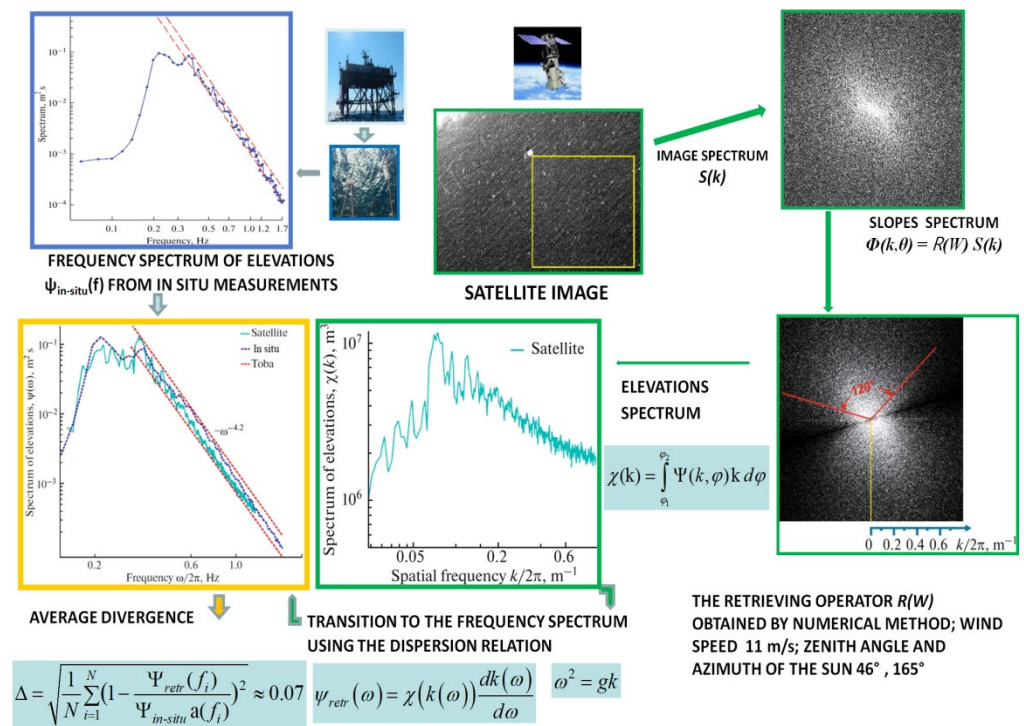


Figure 1. Illustration for the validation method of remote methods for measuring wave spectra by recalculation and comparison with the in situ data where $\omega = f \cdot 2\pi$ is the circular frequency.

The spectral densities obtained in situ are represented by a one-dimensional frequency or frequency-angle dependence. To obtain a similar dependence from a two-dimensional spectrum measured remotely, it is necessary to change to a one-dimensional spatial spectrum and change from spatial to temporal frequencies. To obtain an integral

one-dimensional spectrum, the two-dimensional spatial spectrum is integrated over the wave azimuth:

$$\chi(k) = \int_{\varphi_1}^{\varphi_2} \Psi(k, \varphi) k d\varphi, \quad (23)$$

Physically, a one-dimensional spatial spectrum is the total power of waves with wave number, k , and wavelength, $\lambda = 2\pi/k$, regardless of the direction of their propagation.

For the transition from spatial to temporal frequencies, the deep-water dispersion relation of waves is used. For gravity waves (wavelength more than ~ 0.1 m), it is possible to use the dispersion relation (21). The condition of energy balance in an arbitrary elementary volume makes it possible to change to the frequency dependence:

$$\psi(\omega) = \chi(k(\omega)) \frac{dk}{d\omega}. \quad (24)$$

In this work, the proposed method was used to solve the following main tasks:

- Comparing the properties of the temporal and spatial wave spectra, in particular, the change in the parameters of the power-law approximation in various frequency ranges as well as the integral wave energy.
- Additional validation of the wave spectrum retrieval method from satellite images under conditions of a changing power law of spectrum decay.

3. Results

3.1. Satellite Data Processing Results

3.1.1. Satellite Data

The experimental verification of the described method was carried out according to the data obtained in the Black Sea near the village of Katsiveli ($44^{\circ}23'35''\text{N}$, $33^{\circ}59'04''\text{E}$). The survey of the test region of the water area was carried out from the WorldView-3 satellite with a spatial resolution of 0.4 m.

Figure 2 shows a fragment of the used satellite image with a hydrophysical platform, where complex experiments were carried out. The survey took place on 20 September 2021, 11:34 local time. The azimuth angle of the Sun at the shooting moment was 157.5 degrees, and the elevation angle was 44.5 degrees.

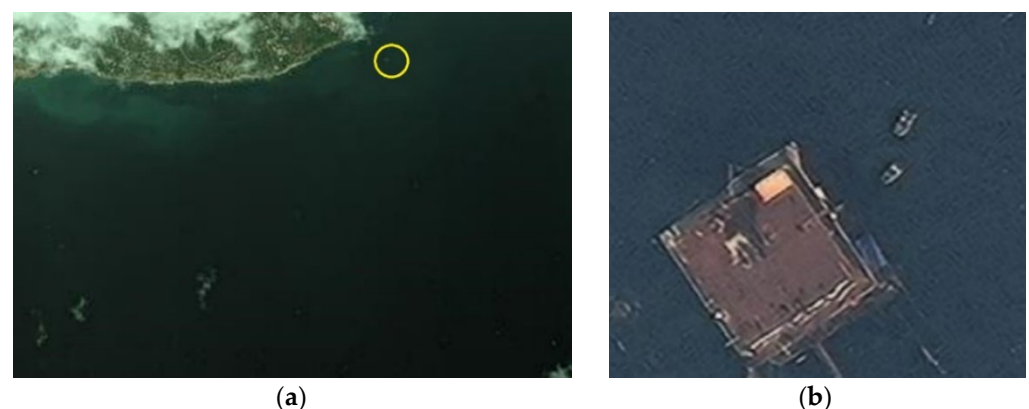


Figure 2. (a) Quicklook of a test WorldView-3 image obtained on 20 September 2021. The position of the hydrophysical platform, where complex experiments were carried out, is marked with yellow; (b) enlarged view of the hydrophysical platform.

To retrieve the wave spectra, we used square sections of a satellite image fragment with sides of 1024, 2048, 4096, and 8192 pixels (see Figure 3).

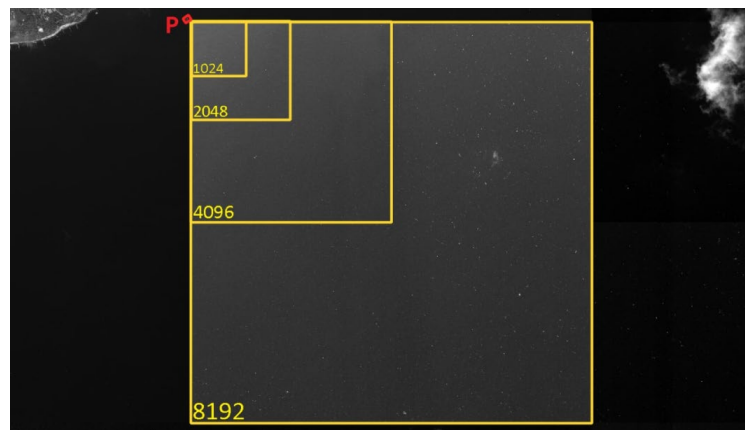


Figure 3. Fragment of the test satellite image. Fragments of different sizes used to retrieve the spectra are marked with yellow. The hydrophysical platform is marked with red.

3.1.2. Wave Spectra Measured from Satellite Data

Figure 4 shows a panorama of the slope spectra retrieved from satellite image fragments using the method described in Section 2.1. The spectra retrieved from the selected fragments are shown at their locations. Due to the discrete nature of the data, the discrete Fourier transform was used to obtain spectral densities of satellite image fragments. One can notice visual differences in the spectra (see Figure 4), which indicates the spatial heterogeneity of sea waves.

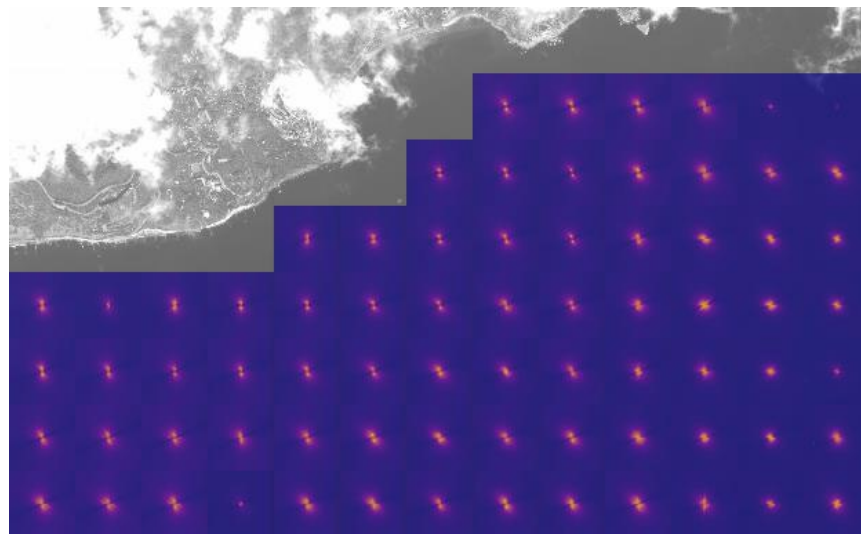


Figure 4. Panorama of the slope spectra. Slope spectra retrieved from 1024×1024 pixel (410×410 m) fragments are shown at the locations of the original satellite image fragments.

For comparison with sea truth data, we transformed the obtained 2D spectra into frequency spectra using Equations (23) and (24). At the same time, in order to eliminate computational errors in the values of spectral density for the wave vector near the directions orthogonal to ϕ_C , which are greatly distorted, an angular sector of 140 degrees was used as an integration region.

Figure 5 shows the integrated spectral density versus frequency for fragments of different sizes: 1024×1024 pixels (0.4×0.4 km), 2048×2048 pixels (0.8×0.8 km), 4096×4096 pixels (1.6×1.6 km), 8192×8192 pixels (3.2×3.2 km).

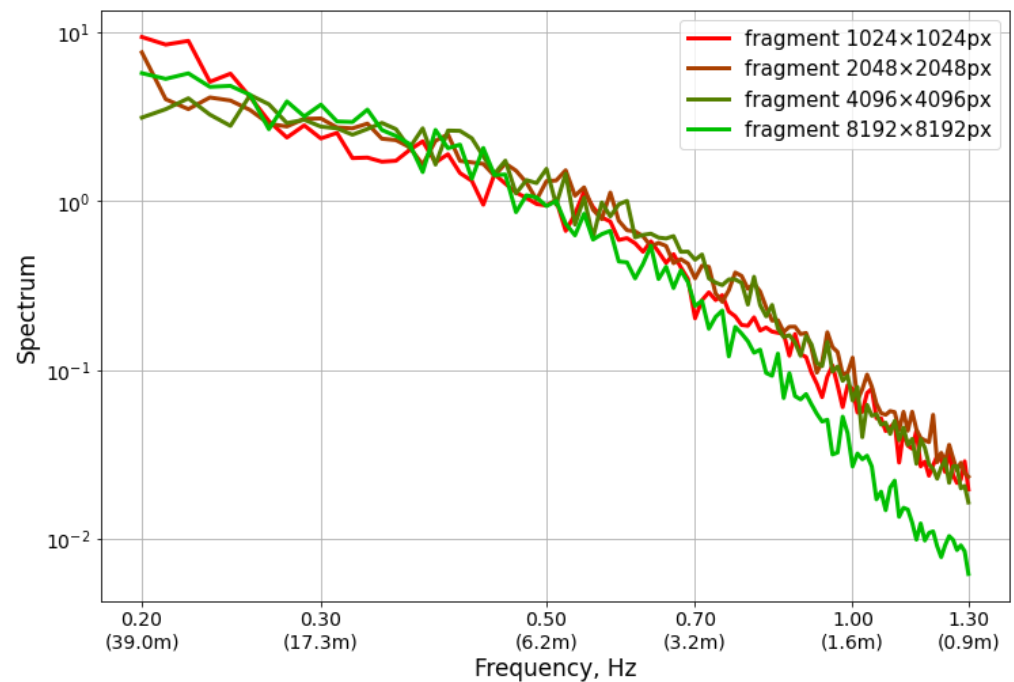


Figure 5. One-dimensional spectra for fragments of different sizes near the platform. For greater clarity, the horizontal axis has two types of labels: frequency and wavelength. Vertical and horizontal axes have a logarithmic scale.

To estimate the decay of spectral density with increasing frequency, it is customary to use the exponent of the power-law approximation of the spectrum for different frequency ranges. Examples of the measurement results of such an indicator for square image fragments with a side of 1024×1024 pixels, corresponding to areas of the sea surface near the platform for four different frequency ranges, are shown in Figure 6. The measurement results are presented as panoramas, where the values of the exponent of the power-law approximation of the elevation spectrum, calculated by Equation (23) for different frequency ranges, are superimposed on a fragment of the satellite image in the area of the platform.

Table 1 shows the average values for all of the presented fragments.

According to the data given in the figures and in the table, it can be concluded that for waves near the platform, there is a transition of a power-law decay of the spectra from -4 to -5 in the vicinity of a frequency of 0.8 Hz, which corresponds to a wavelength of 2.44 m.

Near a frequency of 0.4 Hz, there was also a noticeable change in the spectrum approximation index. A more detailed analysis is given below in Section 3.1.

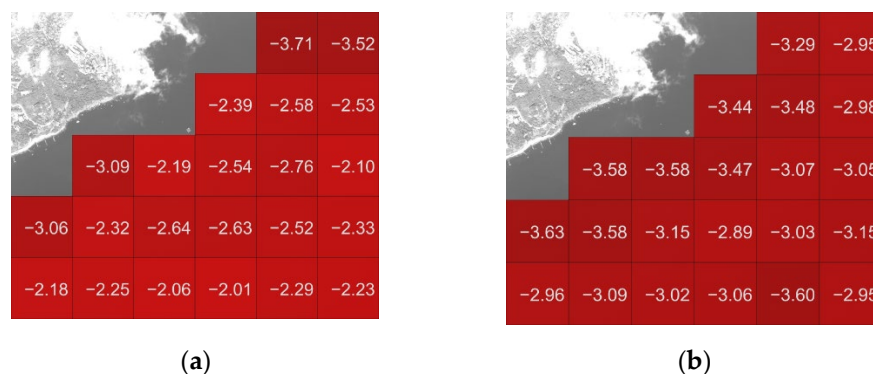


Figure 6. Cont.

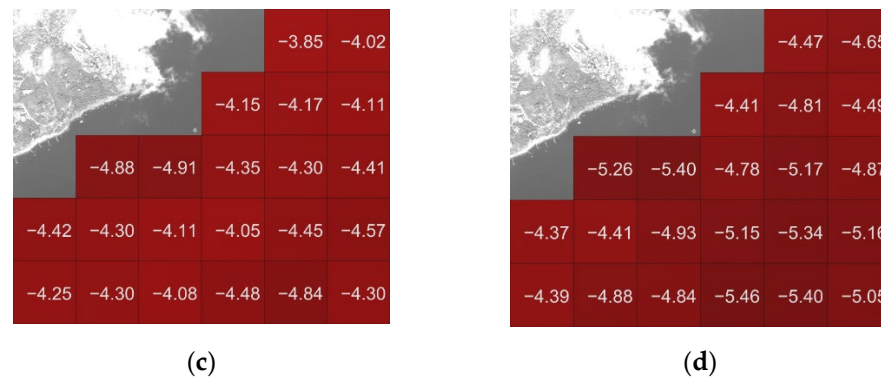


Figure 6. Panorama of the wave spectra. Power-law approximation exponents in different parts of the one-dimensional (integral) spectrum: (a) for 0.25–0.50 Hz; (b) for 0.4–0.8 Hz; (c) for 0.6–1.0 Hz; (d) for 0.8–1.2 Hz. The coefficients are shown at the locations of the original fragments of the satellite image.

Table 1. Spatially averaged coefficients of the power-law decay of the spectra for different frequency ranges.

Frequency Range	Wavelength Range	Exponent
0.25–0.50	6.2–25	–2.54
0.4–0.8	2.44–9.75	–3.23
0.60–1.00	1.55–4.35	–4.33
0.80–1.20	1.1–2.44	–4.90

3.2. Sea Truth Data Processing Results

3.2.1. Data

To validate the method, sea truth measurements were performed from the Black Sea Research Platform of the Marine Hydrophysical Institute of the Russian Academy of Sciences. It is located near the village of Katsiveli, about 500 m from the coast, where the sea depth is about 30 m (in yellow circle in Figure 2). The platform has usually been used for wave studies [21,30–34] and sea truth measurements [15,16,19,20]

Surface waves were measured using an array of six string wave recorders located at the corners and the center of a regular pentagon with a circumscribed radius of 0.25 m. For a detailed description of the wave measuring system, see [30,35]. Sea surface elevations were recorded at a frequency of 10 Hz. The wind speed and direction at the 23 m horizon, air temperature and humidity at the 19 m horizon, and the water temperature in the upper layer of the sea (sensor depth of about 1 m) were recorded from the platform with 1 min averaging using the Davis 6152EU meteorological station. The wind velocity at a standard 10 m horizon and the friction velocity were calculated from the meteorological measurements according to the algorithm [36].

A digital camera performed video recording of the sea surface with a recording frequency of 50 Hz and a resolution of 1920 × 1080 pixels. The camera was installed on a platform at a height of 12 m with a tilt angle of 37 degrees to the horizon, which provided a resolution of about 2 cm on the sea surface. The video record was used to estimate the current velocity vector in the near-surface water layer from the dispersion relation of gravity-capillary waves [21,32,33,37]. The current velocities at depths of 5, 10, 15, and 20 m were measured by MHI-1308 current recorders operating on the platform in the normal mode; see [38].

3.2.2. General Information about the State of the Sea during the Experiment

Figure 7 shows the wind speed at 10 m, wind direction, and significant wave height during the experiment. At the time of the satellite pass, the near-surface wind speed was 8.34 m/s, the friction velocity was 0.31 m/s, and the wave height was 0.61 m. In the time interval between 8:00–9:00, covering the moment of the satellite’s pass, the stable southwest

wind kept the speed at the same level, the average values were $\langle U_{10} \rangle = 8.1 \text{ m/s}$, and the friction velocity was $\langle u_* \rangle = 0.31 \text{ m/s}$. At the same time, the wave height increased from 0.5 m to a peak value of 0.65 m, reached after the overflight of the satellite. Thus, during the experiment, the evolution of the wave field occurred at a stable wind speed.

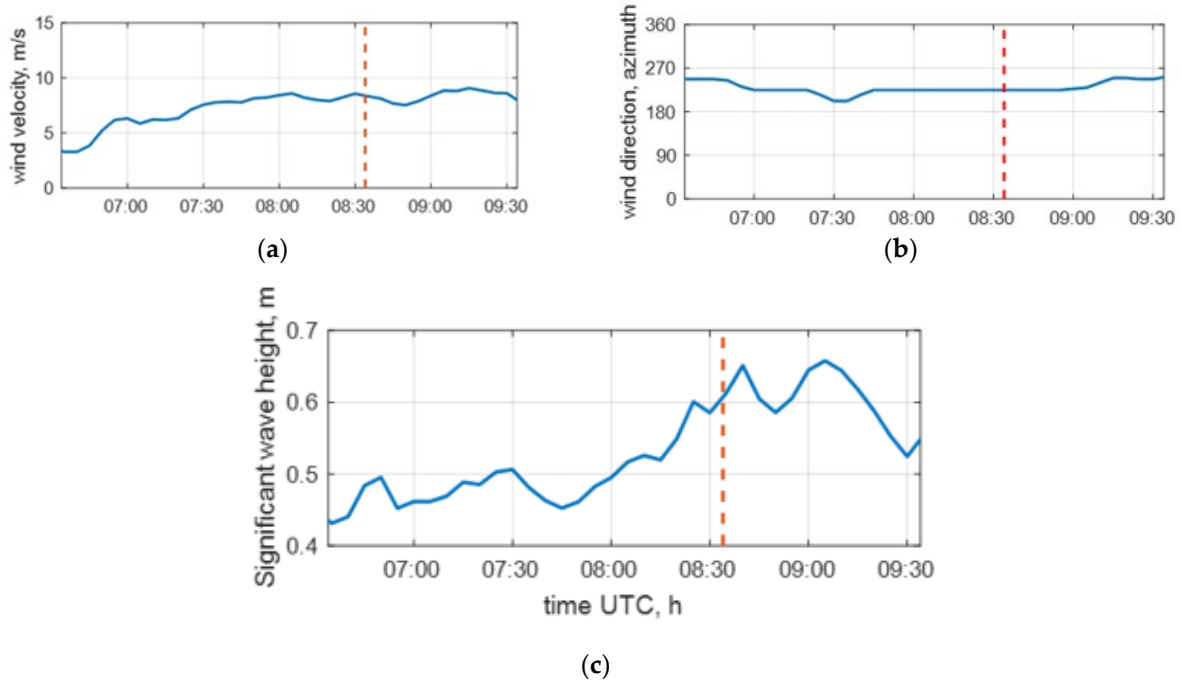


Figure 7. Meteorological conditions of the sea truth experiment: wind speed at the horizon of 10 m (a), wind direction (b); significant wave height (c). The vertical line marks the time of the satellite survey.

3.2.3. Sea Truth Wave Recoding from the Platform to Validate Frequency Spectra

Figure 8 shows the evolution of the wave frequency spectra over a period covering the moment of satellite overflight. The wave spectra were estimated from the recording intervals; periods of survey are given in the legend. While the level of the spectrum in the high-frequency part remained practically unchanged, the wave energy in the peak region increased monotonically, providing the growth of H_s , as shown in Figure 8. If this was due to the development of waves, then the observed H_s increase at a constant wind speed would correspond to a downshifting of the peak frequency, f_p , by 0.27 Hz, as follows from the law of wave development $\frac{\Delta H_s}{H_s} \approx -\frac{3}{2} \frac{\Delta f_p}{f_p}$ (e.g., [30]). Since such a decrease in the frequency of the peak is not clearly observed (see Figure 8), it can be assumed that the increase in wave height is due to the arrival of swell. Hanson and Phillips [39] proposed a method for partitioning the wave spectrum into parts related to swell and wind waves associated with local wind. According to this method, the level of the wind wave spectrum lies within the limits specified by the Toba spectrum [39]:

$$S_T = \frac{\alpha g u_*}{(2\pi)^3 f^4}, \tag{25}$$

where $\alpha = 0.06 \div 0.11$.

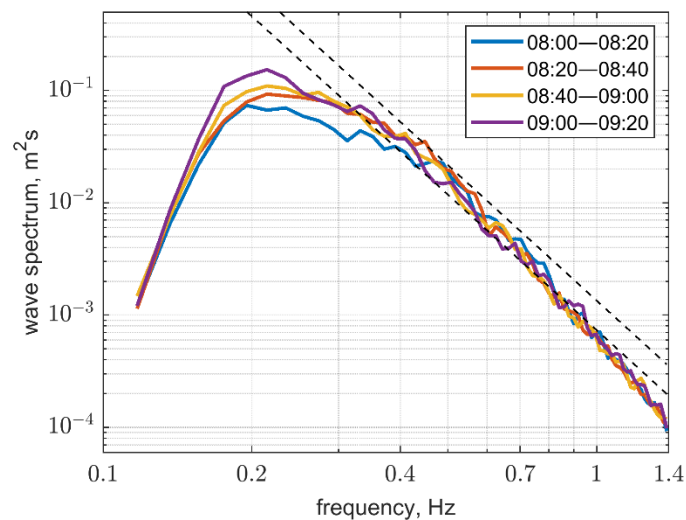


Figure 8. Frequency spectra of waves in the time intervals indicated in the legend. The dashed lines show the level of the “Toba spectrum” according to Equation (25).

As follows from Figure 8, which also shows the limiting levels of the Toba spectrum for the local friction velocity, $u_* = 0.31$ m/s, waves in the vicinity of the spectral peak (with frequencies less than 0.4–0.5 Hz) can be attributed to swell coming to the area of the platform from a distant source. Figure 8 also shows that near the frequency of 0.8 Hz, there was a transition from the f^{-4} spectrum slope to the f^{-5} spectrum slope. Such a transition from an equilibrium spectrum to a saturated spectrum has been discussed in a number of papers (e.g., [40–43]).

3.2.4. Sea Truth Wave Measurements from the Platform for Validating the Angular Characteristics of Wave Spectra Measured from Satellite Data

Figure 9a,b shows the parameters of the angular distribution of waves (i.e., average direction (12), general direction (13), angular width determined by Equations (14) and (15)). Calculation of these parameters for the same time intervals over which the frequency spectra were calculated in Section 3.2.3 did not reveal their obvious changes with time. Therefore, the Figure 9 shows the results obtained from the spectra calculated for the time interval from 8:00 to 9:00 LT.

Figure 9a shows the geographical azimuth of the directions whence the waves came. Waves with frequencies below 0.8 Hz came from the south, and as the frequency increased, the direction of the waves changed to the southwest, in accordance with the southwest wind direction (see Section 3.2.2). Waves of the spectral peak region had the narrowest angular distribution. The width of the angular distribution increased with increasing frequency (see Figure 9b).

Figure 9c shows an estimate of the dispersion relation, $k_*(f)$ (22) compared to the exact theoretical dispersion relation, $k(f)$ (21). The ratio, k_*/k , called the check-ratio, serves as a measure of the quality of determining parameters of the angular distribution, since it, like the parameters of the angular distribution, was obtained using the same spectra [26,27,33].

As follows from Figure 9c, evident deviations occurred in the low frequency region, $f < 0.2$ Hz, and the high frequency region, $f > 1.1$ Hz. The growth in the low-frequency region is associated with the physical absence of wave energy there. In the high-frequency region, as the wavelengths of the studied waves approach the horizontal size of the measuring system, errors of the applied analysis method increase resonantly [31]. In our case, at frequencies $f > 1.1$ Hz, the wavelengths were less than 1.3 m, which was already comparable to the diameter of the wave recorder array of 0.5 m. Thus, we can trust the obtained parameters of the angular distribution of waves only in the frequency range of 0.2–1.1 Hz.

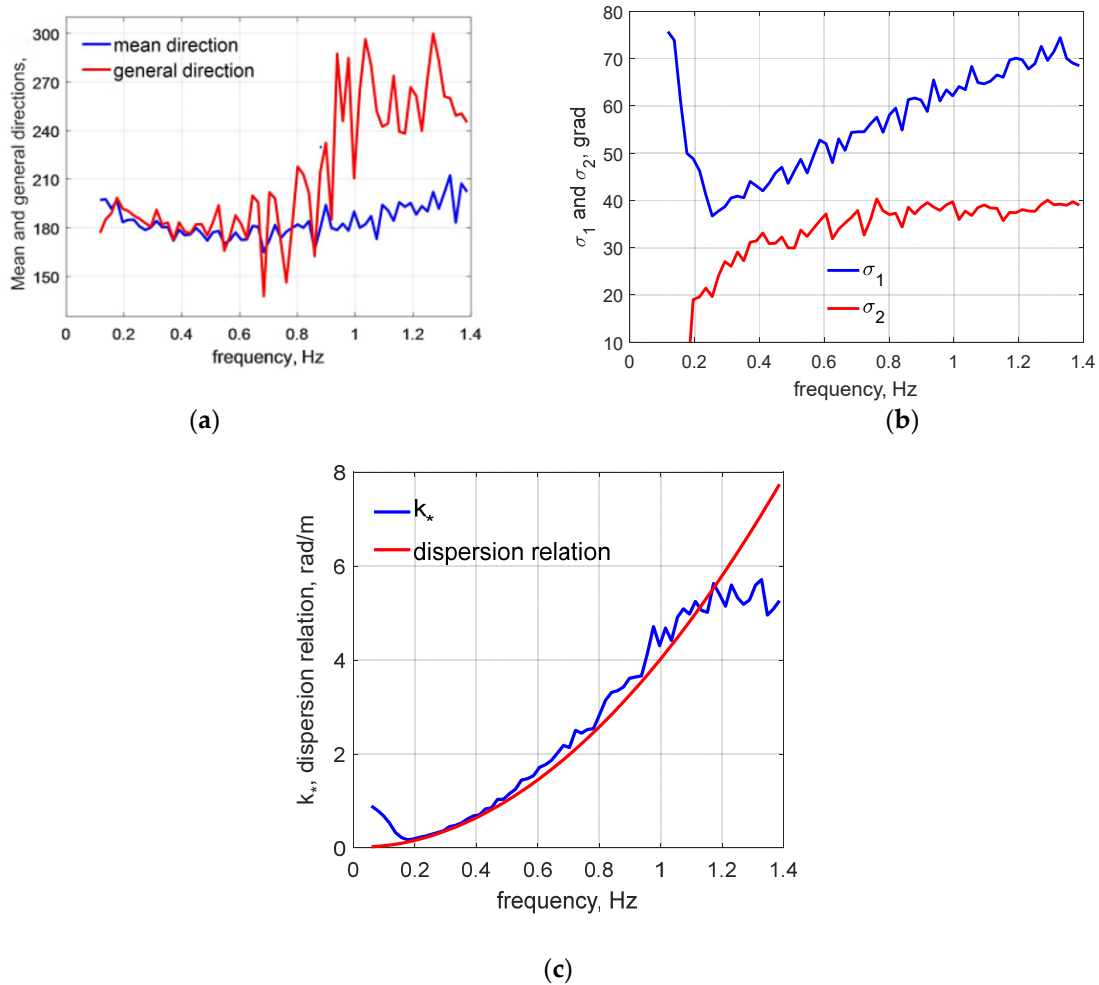


Figure 9. Parameters of the angular distribution of waves: average and general direction of waves (a); angular width of the wave spectrum (b); dispersion relation (c).

3.3. Remote and In Situ Data Comparison Result

To compare with the in situ data, the spatial spectra obtained from the satellite data were recalculated into frequency spectra according to (23) and (24). Fragments of a satellite image of different sizes were used. For each of the sizes, two groups of 121 fragments were processed: one group of fragments was chosen directly near the platform (Figure 10a), and the other was shifted to the southeast so that the centers of the fragments were at a distance of about 1.4 km from the platform. For the transition from the spatial-angular spectrum to the frequency one, according to Equations (24) and (25), an integration sector covering an angle of 140 degrees was used (Figure 10b). The spectra obtained from space images according to the technique described in Section 2 were determined with an accuracy up to a multiplicative constant; therefore, for a correct comparison with the in situ data, normalization by the total energy was used:

$$\Psi_N = \Psi_r \frac{I_c}{I_r}; I_c = \int_{k_l}^{k_h} \Psi_c(k) dk; I_r = \int_{k_l}^{k_h} \Psi_r(k) dk \quad (26)$$

where Ψ_N is the normalized spectrum; Ψ_r is the unnormalized retrieved spectrum; Ψ_c is the measured spectrum; k_l, k_h are the limits, corresponding to the frequency range 0.2–1.1 Hz, within which the dispersion relation (21) is fulfilled.

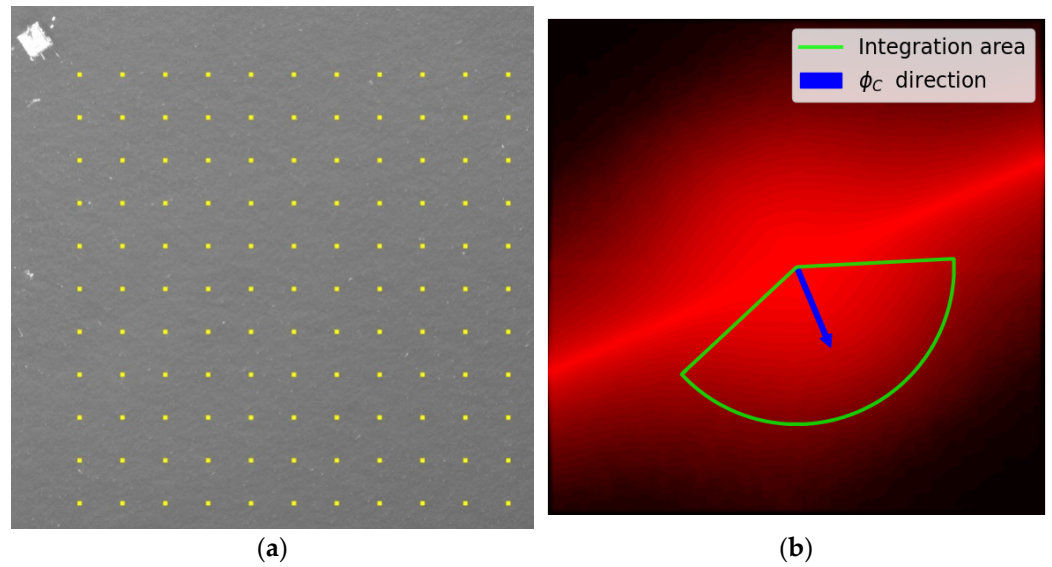


Figure 10. (a) The points near the platform that are upper right corners of the selected fragments. (b) The region of the retrieved spectrum integration. Red background represents a smoothed retrieved elevation spectrum and blue indicates the sun azimuth direction.

Comparison of integral one-dimensional spectra retrieved from satellite images with spectra obtained from in situ data processing is presented on Figure 11. Comparison results obtained with different sizes of image fragments are shown.

For quantitative assessment of the recovery performance, we considered the root mean square percentage error (RMSPE), mean absolute percentage error (MAPE), coefficient of determination (R^2), and logarithmic mean absolute error (LMAE):

$$\text{RMSPE}(\Psi_c, \Psi_N) = \sqrt{\mathbb{E}[(1 - \Psi_N/\Psi_c)^2]} \tag{27}$$

$$\text{MAPE}(\Psi_c, \Psi_N) = \mathbb{E}[|1 - \Psi_N/\Psi_c|] \tag{28}$$

$$R^2(\Psi_c, \Psi_N) = 1 - \frac{\mathbb{D}[\Psi_c - \Psi_N]}{\mathbb{D}[\Psi_c]} \tag{29}$$

$$\text{LMAE}(\Psi_c, \Psi_N) = \mathbb{E}[|\log_{10} \Psi_N(f_i) - \log_{10} \Psi_c(f_i)|] \tag{30}$$

where \mathbb{E} and \mathbb{D} is the sample mean and variance, calculated for a set of frequencies f_1, \dots, f_N .

The calculation results for measures 27–30 are presented in Table 2. Additionally, Table 3 shows the values of measures in four different frequency ranges. The center of the 8192-pixel-side fragment is located at a distance of about 1.4 km, so only one measurement was made for it. Consideration of larger fragments is difficult because of clouds in the image as well as due to high computational expenses. The measures in Tables 2 and 3 were calculated in the frequency interval from 0.2 to 1.2 Hz. The values, f_1, \dots, f_N , were set in the form of a uniform grid with a step of about 0.0195. For comparison, we used the spectrum obtained using string wave buoys corresponding to a 8:20–8:40 LT time interval. Tables 2 and 3 show that as the frequency increased, the divergence of the spectra increased, which may be due to the limited resolution of the satellite image. It can also be noted that, on average, there was a tendency for the decrease in divergence with increasing fragment size. Let us try to give a possible explanation of this pattern. As can be seen in Figure 8, the spectral density of waves has undergone changes. In this case, the spectrum obtained

in situ aggregates data in 20 min. At the same time, as is known, the wave group velocity, which determines the speed of energy movement, is given by Equation (31)

$$v_{gr} = \frac{1}{2} \sqrt{\frac{g}{k}} = \frac{g}{4\pi f} \tag{31}$$

where it follows that for the frequency $f = 0.2$ Hz, the group velocity $v_{gr} \approx 3.9$ m/s and, therefore, in 20 min, the energy can be transferred by waves over a distance of approximately 4.7 km, which is greater than the size of an extended fragment with a side of 3 km. Thus, under conditions of changing waves, smaller fragments may not contain most of the information that was taken into account when constructing the spectrum using in situ data. Based on the above, a fragment with a side of about 3 km is the most adequate option for method validation with the in situ data averaged over 20 min.

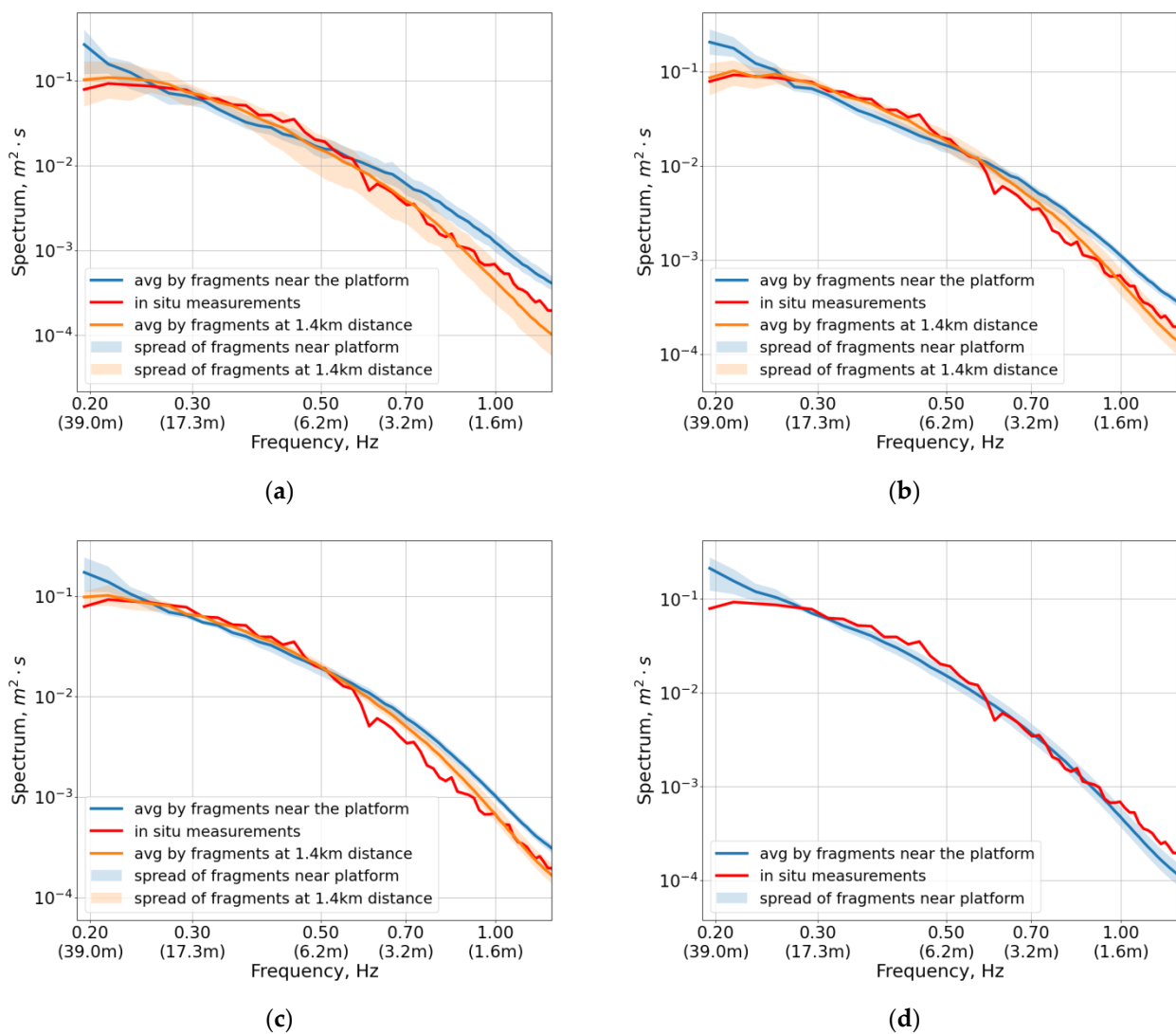


Figure 11. Comparison of integral one-dimensional spectra retrieved from satellite images with the integral spectrum obtained from in situ data processing. Fragment sizes 1024 (a), 2048 (b), 4096 (c), 8192 (d).

Table 2. Values of different quantitative measures of recovery performance in the range of 0.2–1.2 Hz.

Fragment	RMSPE	MAPE	R ²	LMAE
1024 np *	0.805	0.683	0.815	0.218
1024 dfp **	0.237	0.196	0.967	0.096
2048 np	0.676	0.584	0.737	0.196
2048 dfp	0.231	0.176	0.989	0.072
4096 np	0.619	0.519	0.913	0.173
4096 dfp	0.293	0.206	0.988	0.077
8192 np	0.234	0.190	0.849	0.090

* np—fragments near the platform. ** dfp—fragments at 1.4 km distance

Table 3. Values of different quantitative measures of recovery performance in diverse frequency ranges.

Fragment	0.25–0.50 Hz				0.40–0.80 Hz			
	RMSPE	MAPE	R ²	LMAE	RMSPE	MAPE	R ²	LMAE
1024 np	0.239	0.219	0.719	0.111	0.585	0.475	0.803	0.167
1024 dfp	0.165	0.143	0.875	0.068	0.198	0.159	0.882	0.071
2048 np	0.245	0.231	0.675	0.115	0.525	0.433	0.789	0.157
2048 dfp	0.105	0.080	0.949	0.037	0.277	0.212	0.940	0.082
4096 np	0.156	0.137	0.845	0.066	0.582	0.463	0.891	0.156
4096 dfp	0.096	0.074	0.944	0.034	0.364	0.282	0.951	0.103
8192 np	0.192	0.172	0.819	0.083	0.191	0.151	0.855	0.070
Fragment	0.60–1.00 Hz				0.80–1.20 Hz			
	RMSPE	MAPE	R ²	LMAE	RMSPE	MAPE	R ²	LMAE
1024 np	1.003	0.962	−0.64	0.288	1.094	1.080	−4.334	0.317
1024 dfp	0.192	0.150	0.858	0.065	0.304	0.271	0.835	0.144
2048 np	0.850	0.817	−0.291	0.255	0.885	0.868	−2.733	0.270
2048 dfp	0.320	0.270	0.594	0.100	0.232	0.199	0.608	0.085
4096 np	0.851	0.825	−0.737	0.258	0.765	0.736	−2.363	0.236
4096 dfp	0.442	0.396	0.272	0.141	0.283	0.203	0.266	0.076
8192 np	0.152	0.112	0.911	0.048	0.252	0.221	0.885	0.113

Table 4 shows the coefficients of the power-law decay of the spectra for different frequency ranges.

Table 4. Coefficients of the power-law decay of the spectra for different fragments and frequency ranges.

Fragment \ Frequency	0.25–0.50 Hz	0.40–0.80 Hz	0.60–1.00 Hz	0.80–1.20 Hz
1024 np	−2.6	−2.9	−4.4	5.1
1024 dfp	−2.8	4.0	−5.9	−6.7
2048 np	−2.7	−3.1	−4.5	−5.2
2048 dfp	−2.5	−4.1	−5.5	−6.6
4096 np	−2.2	−3.4	−4.8	−5.6
4096 dfp	−2.1	−4.0	−5.4	−6.5
8192 np	−2.7	−4.1	−5.5	−6.5
In situ measurements	−2.3	−4.9	−5.2	−4.9

3.4. Studying Spectra of Spatially-Inhomogeneous Waves

To study the spatial variability of the wave spectra, we considered the spectra of satellite image fragments at different distances from the platform. The results of remote measurements performed by the developed method can be easily presented as polar diagrams that display the integral characteristics of waves. The following approach was used to build diagrams. First, the pole of the diagram was selected, then, the surrounding horizontal surface, represented by polar coordinates divided into segments by angles and

distances. Finally, for each segment, an average sample characteristic was taken for several fragments with center points located inside the segment. The centers can be selected in various ways. Using the described approach, polar diagrams of the coefficients of wave spectrum exponential decay were obtained in different frequency ranges (Figure 12) as well as a diagram of the integral wave energy near the spectral maximum (Figure 13). The center of the hydrophysical platform was used as a pole. The angular sectors covered the range from 90 to 250 degrees with a step of 20 degrees, and the radial segments covered the distance from 100 m to 3200 m with a step of 400 m. Within each segment, the magnitude value was averaged over four fragments centered at the points dividing the sector by angle and distance into three equal parts. When processing the satellite image described in Section 3.1.1, one of the sectors was excluded because the sea surface was obscured by clouds.

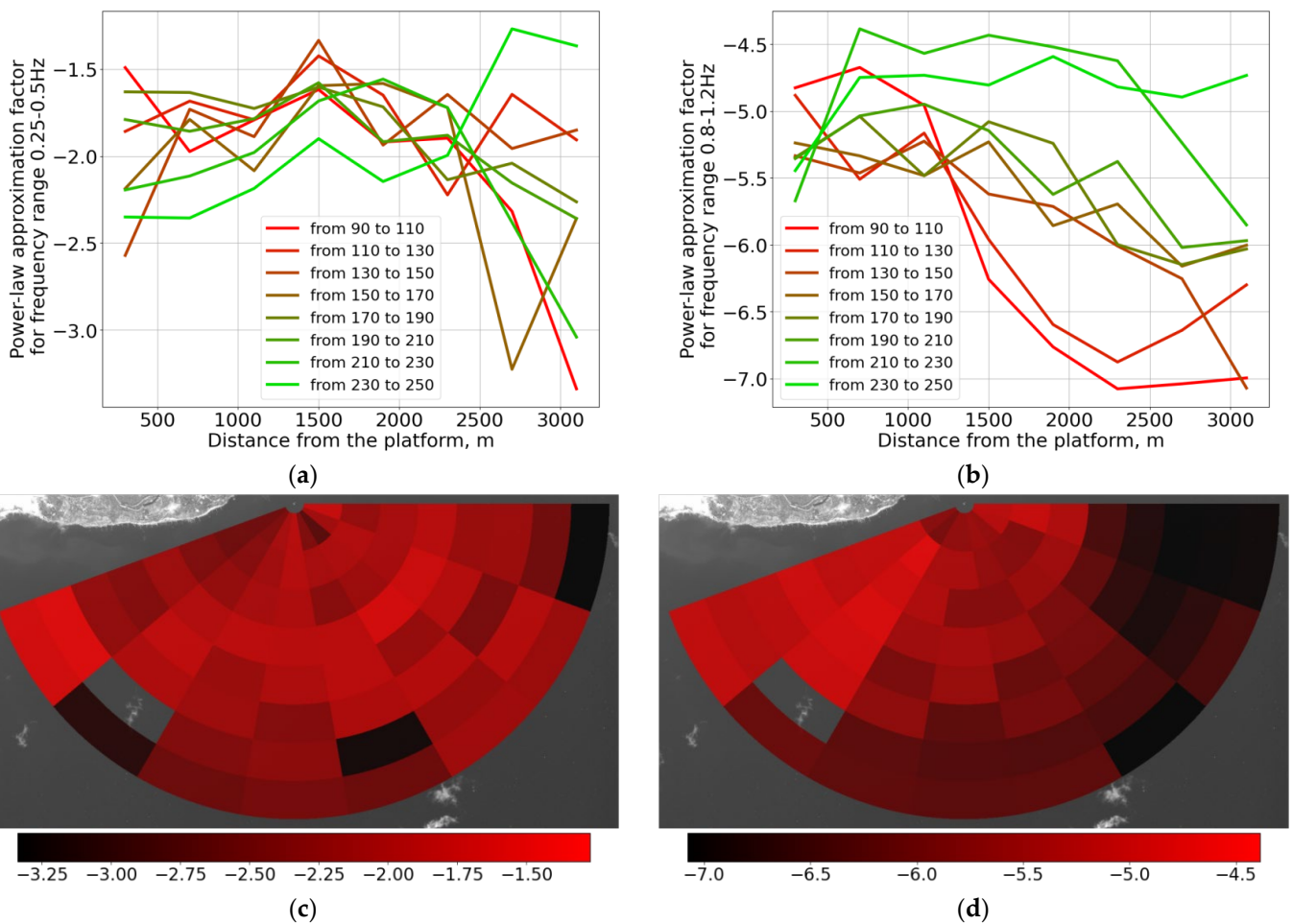


Figure 12. (a,c) Dependence of the exponent of power-law approximation for frequency range of 0.25–0.50 Hz on the distance to the platform in different directions in directional and polar representation; (b,d) Same for frequency ranges 0.8–1.2 Hz; In (b,d) colors characterizing the slope coefficients are superimposed on the location of the segments.

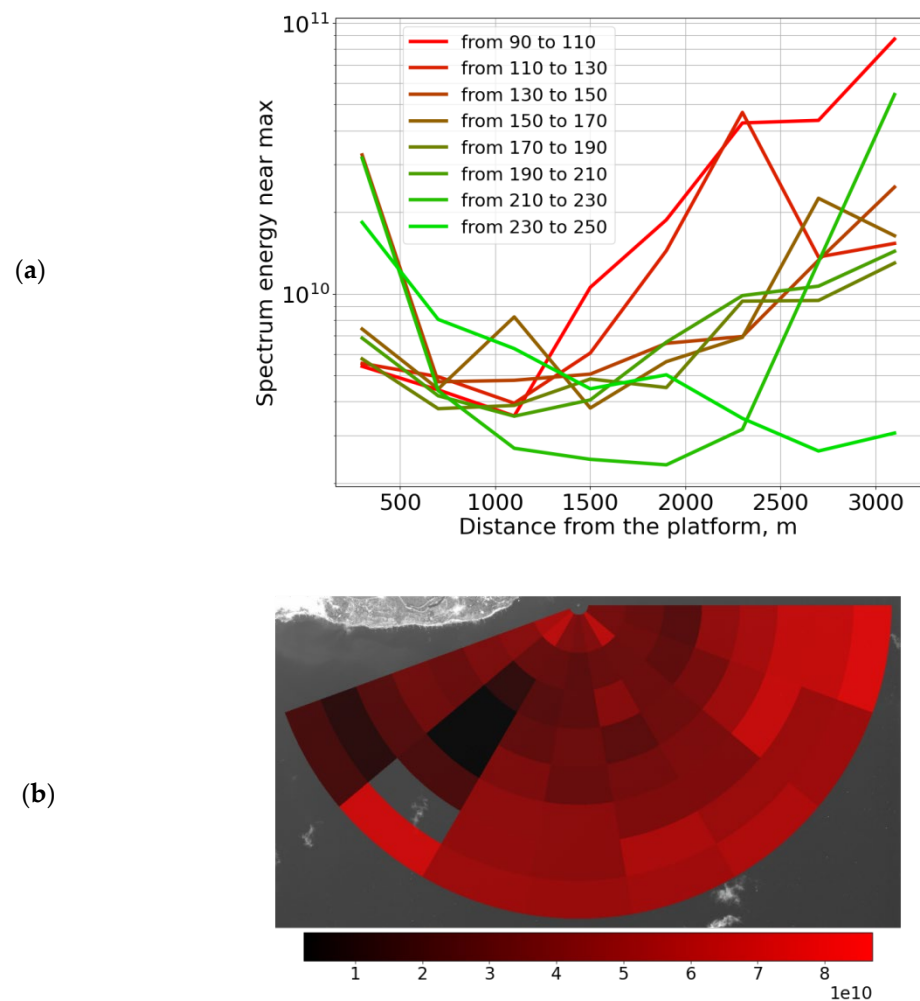


Figure 13. Dependence of integral energy of the wave spectrum near the spectral maximum (frequency 0.2–0.4 Hz) on the direction and distance to the platform. (a) One-dimensional plots along selected directions; (b) two-dimensional polar diagram.

To study the wave spectra depending on the direction, using the dispersion relation (21), a transition was made from the spectrum of elevations depending on the wavenumber, to the spectrum of elevations depending on the frequency and direction of the waves:

$$\psi(f, \phi) = \chi(k(f), \phi) \frac{dk}{df}, \tag{32}$$

4. Discussion

In our experiment, we observed mixed seas consisting of two wave systems. As follows from the in situ measurements, swell coming from the south provided the main contribution to the significant wave height. The second wave system corresponded to wind waves matched with the local wind (see Sections 3.2.3 and 3.2.4). In the frequency spectrum, swell with a spectral peak of about 0.2 Hz passed into wind waves in the vicinity of the frequency of 0.4 Hz. This is expressed as a sharp change in the spectrum decay exponent. For higher frequencies, the spectrum decay exponent grew from about 4 up to 5. The angular distribution of waves showed an increase in angular width with increasing frequency. Such features of the wave spectra have been previously reported in number (see [39–43]). The same features were revealed in the wave spectra measured by the satellite (see Figure 11 and Section 3.4). The wave unsteadiness observed in the contact

measurements (see Figure 8) was expressed in the spatial heterogeneity of the parameters of the waves observed from the satellite (see Section 3.4).

Numerous approaches to retrieving waves from ocean optical image intensity belong to three main groups: (i) using only sun glint area (e.g., [8,9,22,44]); (ii) using a full physical model of wave signatures in optical images (e.g., [16,19,23,24,45]); (iii) variations of a simpler approach based on Equation (4) without accounting for the nonlinear term N (see [6,10,32,46–48] among others). The first group's method is based on strict theory but has practically been applied only to tropical areas. Studies of the third group presented many physically true results, but ignoring the nonlinear terms can result in unexpected errors [48]. Our study belonged to the second group, which uses modeling to process the satellite image. This approach remains challenging but the most prospective for the future.

The specificity of the high-resolution (0.4 m) image used in our study needs discussion. First, it resulted in obtaining a spectrum in a wider range of wavelengths compared with other studies. Theoretically, the ratio of the maximum resolved wavenumber to spectral peak wavenumber achieves more than 36 (see Figure 5), which is greater than in sun glint studies [8,9,22,45] and comparable with the results of photography [47] and polarimetry [32]. Spectra in wide wavenumber range yielded information on spectral shape, number of wave systems in mixed seas, and exponent of spectrum decay (as in the presented study). The spectrum shape can also contain information about the subsurface currents [2] and the presence of pollutants on the sea surface [3,4,6,19].

Second, the high-resolution image led to smaller changes in the viewing angle within the image compared to other studies that used ordinary-resolution images. Those studies evaluated the transfer function, which is analogous to our operator R defined by (5), from the smoothed brightness field (see modern explanation in [46]). This approach is not applicable if changes in the viewing angle within the image are much smaller than the characteristic slope of sea waves. It may be considered as a certain drawback of high resolution. The approach of the second group of research overcomes this difficulty thanks to modeling the physical processes forming satellite images [15,19,24,45]. This article intended to demonstrate it.

5. Conclusions

The principle results of the work are:

- The development and validation of the method of the remote measurement of wave spectra variability related to the spatial and temporal inhomogeneity of waves, which can be used to study the various phenomena on the sea surface;
- Obtaining estimates of the sea spectra parameters from the data of remote measurements, which correspond to the results of sea truth measurements. The development of a method for retrieving the spectra of sea waves to study spatially inhomogeneous waves is of greatest interest.

An analysis of the temporal and spatial variability of the state of sea waves in the test water area was carried out to validate the developed method for studying the variability of sea waves in the coastal zone under conditions of limited current. The spatial spectral characteristics of sea waves, estimated from the remote sensing data, were compared with the corresponding characteristics measured in situ under controlled conditions based on the results of complex experiments. As data on the sea for comparison, we used data from a group of string wave recorders installed on a stationary oceanographic platform of the Black Sea hydrophysical test ground.

Comparison of the wave spectra and their statistical characteristics showed that the results obtained from the processing of high resolution space images and the results of sea truth processing corresponded.

The development of the presented method in retrieving the spectra of sea waves in studying spatially inhomogeneous waves is of great interest.

It is shown that the best agreement between the results of the remote measurement of wave spectra and the data of sea truth measurements averaged over 20 min was achieved

by processing fragments of a satellite image of a sea surface area with a linear size of 3 km. At the same time, the average absolute percentage error according to the satellite data did not exceed 0.2, and the value of the determination coefficient was not less than 0.8. This testifies that the accuracy of remote measurements of sea wave spectra is close to the accuracy of in situ measurements.

A study of spatial variations in the degree of wave spectrum decay was carried out as well as a study of the angular integral spectra of waves. The possibility of changing the power-law decay in the spectrum of developing waves has been experimentally confirmed. In particular, it was found that for waves near the platform, there was a transition of the power-law decay of the spectra from -4 to -5 in the vicinity of a wavelength of 2.44 m (frequency 0.8 Hz). The detected change in decay corresponds to the transition of an equilibrium spectrum to a saturated one.

The angular distribution of waves obtained in this work from remote sensing data corresponds to the results of measurements performed using the data of string wave recorders.

Author Contributions: Conceptualization, A.M., V.D. and V.B.; Methodology, A.M. and V.D.; Software, A.M., V.K., Y.Y. and M.Y.; Validation, A.M., V.D., V.K. and Y.Y.; Formal analysis, V.B., V.D. and A.M.; Investigation, A.M.; Resources, V.B.; Data curation, V.B.; Writing—original draft preparation, A.M., V.D., V.K., Y.Y. and M.Y.; Writing—review and editing, V.B., V.D. and A.M.; Visualization, V.K. and Y.Y.; Supervision, V.B.; Project administration, V.B.; Funding acquisition, V.B. All authors have read and agreed to the published version of the manuscript.

Funding: The satellite survey was carried out with the financial support of the Russian Foundation for Basic Research, MOST (China), and DST (India) in the framework of the Research Project No. 19-55-80021. Sea truth was carried out under the framework of the State Assignment of Marine Hydrophysical Institute of the RAS No. 0555-2021-0005.

Institutional Review Board Statement: Not applicable. The study did not involve humans or animals.

Informed Consent Statement: Not applicable as the study did not involve humans.

Data Availability Statement: The study did not report or generate any data.

Acknowledgments: The authors thank A. Garmashov (Marine Hydrophysical Institute of the RAS, Sevastopol) for data on current velocities at depths of 5–20 m.

Conflicts of Interest: The authors declare no conflict of interest. The funders had no role in the design of the study; in the collection, analyses, or interpretation of data; in the writing of the manuscript, or in the decision to publish the results.

References

1. Phillips, O.M. *The Dynamics of the Upper Ocean*, 2nd ed.; Cambridge University Press: New York, NY, USA, 1977.
2. Ardhuin, F.; Stopa, J.E.; Chapron, B.; Collard, F.; Husson, R.; Jensen, R.E.; Johannessen, J.; Mouche, A.; Passaro, M.; Quartly, G.D.; et al. Observing Sea States. *Front. Mar. Sci.* **2019**, *6*, 124. [CrossRef]
3. Bondur, V.G. Aerokosmicheskie metody v sovremennoy okeanologii (Aerospace methods in modern oceanology). In *New Ideas in Oceanology*; V.1. Physics. Chemistry. Biology; Nauka: Moscow, Russia, 2004; pp. 55–117. (In Russian)
4. Bondur Valery, G. Satellite monitoring and mathematical modelling of deep runoff turbulent jets in coastal water areas. In *Waste Water—Evaluation and Management*; InTech: Rijeka, Croatia, 2011; pp. 155–180. ISBN 978-953-307-233-3. Available online: <http://www.intechopen.com/articles/show/title/satellite-monitoring-and-mathematical-modelling-of-deep-runoff-turbulent-jets-in-coastal-water-areas> (accessed on 28 September 2022). [CrossRef]
5. Bondur, V.G.; Vorobjev, V.E.; Grebenjuk, Y.V.; Sabinin, K.D.; Serebryany, A.N. Study of fields of currents and pollution of the coastal waters on the Gelendzhik Shelf of the Black Sea with space data. *Izv. Atmos. Ocean. Phys.* **2013**, *49*, 886–896. [CrossRef]
6. Dulov, V.A.; Yurovskaya, M.V. Spectral Contrasts of Short Wind Waves in Artificial Slicks from the Sea Surface Photographs. *Phys. Oceanogr.* **2021**, *28*, 348–360. [CrossRef]
7. Jiao, P.; Matin Nazar, A.; Egbe, K.-J.I.; Barri, K.; Alavi, A.H. Magnetic capsule triboelectric nanogenerators. *Sci. Rep.* **2022**, *12*, 1–10. [CrossRef]
8. Yurovskaya, M.; Kudryavtsev, V.; Chapron, B.; Collard, F. Ocean surface current retrieval from space: The Sentinel-2 multispectral capabilities. *Remote Sens. Environ.* **2019**, *234*, 111468. [CrossRef]
9. Ardhuin, F.; Alday, M.; Yurovskaya, M. Total surface current vector and shear from a sequence of satellite images: Effect of waves in opposite directions. *J. Geophys. Res. Ocean.* **2021**, *126*, e2021JC017342. [CrossRef]

10. Leu, L.-G.; Kuo, Y.-Y.; Liu, C.-T. Coastal Bathymetry from the Wave Spectrum of Spot Images. *Coast. Eng. J.* **1999**, *41*, 21–41. [[CrossRef](#)]
11. Ardhuin, F.; Gille, S.T.; Menemenlis, D.; Rocha, C.B.; Rasche, N.; Chapron, B.; Gula, J.; Molemaker, J. Small-scale open ocean currents have large effects on wind wave heights. *J. Geophys. Res. Ocean.* **2017**, *122*, 4500–4517. [[CrossRef](#)]
12. Wang, J.; Bethel, B.J.; Dong, C.; Li, C.; Cao, Y. Numerical Simulation and Observational Data Analysis of Mesoscale Eddy Effects on Surface Waves in the South China Sea. *Remote Sens.* **2022**, *14*, 1463. [[CrossRef](#)]
13. Hauser, D.; Tison, C.; Amiot, T.; Delaye, L.; Corcoral, N.; Castellan, P. SWIM: The first spaceborne wave scatterometer. *IEEE Trans. Geosci. Remote Sens.* **2017**, *55*, 3000–3014. [[CrossRef](#)]
14. Ardhuin, F.; Aksenov, Y.; Benetazzo, A.; Bertino, L.; Brandt, P.; Caubet, E.; Chapron, B.; Collard, F.; Cravatte, S.; Delouis, J.M.; et al. Measuring currents, ice drift, and waves from space: The sea surface kinematics multiscale monitoring (SKIM) concept. *Ocean Sci.* **2018**, *14*, 337–354. [[CrossRef](#)]
15. Bondur, V.G.; Muryinin, A.B. Methods for retrieval of sea wave spectra from aerospace image spectra. *Izv. Atmos. Ocean. Phys.* **2016**, *52*, 877–887. [[CrossRef](#)]
16. Bondur, V.G.; Dulov, V.A.; Muryinin, A.B.; Yurovsky, Y.Y. A study of sea-wave spectra in a wide wavelength range from satellite and in-situ data. *Izv. Atmos. Ocean. Phys.* **2016**, *52*, 888–903. [[CrossRef](#)]
17. Bondur, V.G.; Vorobyev, V.E.; Muryinin, A.B. Retrieving Sea Wave Spectra Based on High-Resolution Space Images under Different Conditions of Wave Generation. *Izv. Atmos. Ocean. Phys.* **2020**, *56*, 887–897. [[CrossRef](#)]
18. Vorobyev, V.E.; Muryinin, A.B. Retrieving Spectra of Spatially Inhomogeneous Sea Waves during the Satellite Monitoring of Vast Water Areas. *Izv. Atmos. Ocean. Phys.* **2021**, *57*, 1108–1116. [[CrossRef](#)]
19. Bondur, V.; Muryinin, A. The Approach for Studying Variability of SeaWave Spectra in a Wide Range of Wavelengths from High-Resolution Satellite Optical Imagery. *J. Mar. Sci. Eng.* **2021**, *9*, 823. [[CrossRef](#)]
20. Bondur, V.G.; Dulov, V.A.; Muryinin, A.B.; Ignatiev, V.Y. Retrieving Sea-Wave Spectra Using Satellite-Imagery Spectra in a Wide Range of Frequencies. *Izv. Atmos. Ocean. Phys.* **2016**, *52*, 637–648. [[CrossRef](#)]
21. Yurovsky, Y.Y.; Kudryavtsev, V.N.; Grodsky, B.; Chapron, S.A. Validation of Doppler Scatterometer Concepts using Measurements from the Black Sea Research Platform. In Proceedings of the 2018 Doppler Oceanography from Space (DOFS), Brest, France, 10–12 October 2018; pp. 1–9. [[CrossRef](#)]
22. Yurovskaya, M.; Kudryavtsev, V.; Chapron, B.; Rasche, N.; Collard, F. Wave Spectrum and Surface Current Retrieval from Airborne and Satellite SunGlitter Imagery. In Proceedings of the IGARSS 2018—2018 IEEE International Geoscience and Remote Sensing Symposium, Valencia, Spain, 22–27 July 2018. [[CrossRef](#)]
23. Muryinin, A.B. Sea Surface 2-D Spectra Recovered from Optical Images in Nonlinear Radiance Model. *Issled. Zemli Kosm.* **1990**, *6*, 60–70. (In Russian)
24. Bondur, V.G.; Muryinin, A.B. Vosstanovlenie spektrov poverkhnostnogo volneniya po spektram izobrazheniy s uchetom nelineynoy modulyatsii polya yarkosti (Restoration of surface waves spectra from the spectra of images with the account for nonlinear modulation of the brightness field). *Opt. Atmos. Okeana* **1991**, *4*, 387–393. (In Russian)
25. Earle, M. Nondirectional and Directional Wave Data Analysis Procedures; NDBC Technical Document 96-01. Available online: www.ndbc.noaa.gov/wavemeas.pdf (accessed on 3 July 2021).
26. Longuet-Higgins, M.; Cartwright, D.; Smith, N. Observations of the directional spectrum of sea waves using the motions of a floating buoy. In *Ocean Wave Spectra*; Prentice-Hall: Hoboken, NJ, USA, 1963; pp. 111–136.
27. Krogstad, H.E. Conventional analysis of wave measurement arrays. In *Measuring and Analysing the Directional Spectra of Ocean Waves*; Hauser, D., Kahma, K.K., Krogstad, H.E., Lehner, S., Monbaliu, J., Wyatt, L.R., Eds.; Office for Official Publications of the European Communities: Luxembourg, 2005; pp. 56–71.
28. Kuik, A.J.; van Vledder, G.P.; Holthuijsen, L.H. A method for the routine analysis of pitch-and-roll buoy wave data. *J. Phys. Oceanogr.* **2002**, *18*, 1020–1034. [[CrossRef](#)]
29. Bendat, J.; Piersol, A. *Random Data: Analysis and Measurement Procedures*, 4th ed.; John Wiley & Sons: Hoboken, NJ, USA, 2010. [[CrossRef](#)]
30. Dulov, V.; Kudryavtsev, V.; Skiba, E. On fetch- and duration-limited wind wave growth: Data and parametric model. *Ocean Model.* **2020**, *153*, 101676. [[CrossRef](#)]
31. Yurovsky, Y.Y.; Dulov, V.A. MEMS-based wave buoy: Towards short wind-wave sensing. *Ocean. Eng.* **2020**, *217*, 108043. [[CrossRef](#)]
32. Leckler, F.; Ardhuin, F.; Peureux, C.; Benetazzo, A.; Bergamasco, F.; Dulov, V. Analysis and interpretation of frequency-wavenumber spectra of Young wind waves. *J. Phys. Oceanogr.* **2015**, *45*, 2484–2496. [[CrossRef](#)]
33. Smeltzer, B.K.; Æsøy, E.; Ådnøy, A.; Ellingsen, S.Å. An improved method for determining near-surface currents from wave dispersion measurements. *J. Geophys. Res. Ocean.* **2019**, *124*, 8832–8851. [[CrossRef](#)]
34. Baranovskii, V.D.; Bondur, V.G.; Kulakov, V.V. Calibration of remote measurements of 2-D spatial wave spectra from optical images. *Issled. Zemli Kosm.* **1992**, *2*, 59–67. (In Russian)
35. Shokurov, M.V.; Dulov, V.A.; Skiba, E.V.; Smolov, V.E. Wind waves in the coastal zone of the southern crimea: Assessment of simulation quality based on in situ measurements. *Oceanology* **2016**, *56*, 214–225. [[CrossRef](#)]
36. Fairall, C.W.; Bradley, E.F.; Hare, J.E.; Grachev, A.A.; Edson, J.B. Bulk parameterization of air-sea fluxes: Updates and verification for the COARE algorithm. *J. Clim.* **2003**, *16*, 571–591. [[CrossRef](#)]

37. Laxague, N.J.M.; Haus, B.K.; Ortiz-Suslow, D.G.; Smith, C.J.; Novelli, G.; Dai, H.; Ozgokmen, T.; Graber, H.C. Passive optical sensing of the near-surface wind-driven current profile. *J. Atmos. Ocean. Technol.* **2017**, *34*, 1097–1111. [[CrossRef](#)]
38. Kuznetsov, A.S. Mean Long-Term Seasonal Variability of the Coastal Current at the Crimea Southern Coast in 2002–2020. *Phys. Oceanogr.* **2022**, *29*, 139–151. Available online: <http://physical-oceanography.ru/repository/2022/2/2.html> (accessed on 28 September 2022). [[CrossRef](#)]
39. Hanson, J.L.; Phillips, O.M. Wind sea growth and dissipation in the open ocean. *J. Phys. Oceanogr.* **1999**, *29*, 1633–1648. [[CrossRef](#)]
40. Toba, J. Local balance in the air-sea boundary process. *Oceanogr. Soc. Japan.* **1973**, *29*, 209–225. [[CrossRef](#)]
41. Donelan, M.A.; Hamilton, J.; Hui, W.H. Directional Spectra of Wind-Generated Waves. *Philos. Trans. R. Soc. A Math. Phys. Eng. Sci.* **1985**, *315*, 509–562. [[CrossRef](#)]
42. Lenain, L.; Melville, W.K. Measurements of the Directional Spectrum across the Equilibrium Saturation Ranges of Wind-Generated Surface Waves. *J. Phys. Oceanogr.* **2017**, *47*, 2123–2138. [[CrossRef](#)]
43. Romero, L.; Melville, W.K. Airborne Observations of Fetch-Limited Waves in the Gulf of Tehuantepec. *J. Phys. Oceanogr.* **2010**, *40*, 441–465. [[CrossRef](#)]
44. Gelpi, C.G.; Schuraytz, B.C.; Husman, M.E. Ocean wave height spectra computed from high-altitude, optical, infrared images. *J. Geophys. Res.* **2001**, *106*, 31403–31413. [[CrossRef](#)]
45. Kudryavtsev, V.; Yurovskaya, M.; Chapron, B.; Collard, F.; Donlon, C. Sun glitter imagery of ocean surface waves. Part 1: Directional spectrum retrieval and validation. *J. Geophys. Res. (Oceans)* **2017**, *122*, 1369–1383. [[CrossRef](#)]
46. Almar, R.; Bergsma, E.W.J.; Catalan, P.A.; Cienfuegos, R.; Suarez, L.; Lucero, F.; Lerma, A.N.; Desmazes, F.; Perugini, E.; Palmsten, M.L.; et al. Sea State from Single Optical Images: A Methodology to Derive Wind-Generated Ocean Waves from Cameras, Drones and Satellites. *Remote Sens.* **2021**, *13*, 679. [[CrossRef](#)]
47. Yurovskaya, M.V.; Dulov, V.A.; Chapron, B.; Kudryavtsev, V.N. Directional short wind wave spectra derived from the sea surface photography. *J. Geophys. Res.* **2013**, *118*, 4380–4394. [[CrossRef](#)]
48. Monaldo, F.M.; Kasevich, R.S. Daylight imagery of ocean surface waves for wave spectra. *J. Phys. Oceanogr.* **1981**, *11*, 272–283. [[CrossRef](#)]